Int J CARS
DOI 10.1007/s11548-012-0780-8

ORIGINAL ARTICLE

Generating prostate models by means of geometric deformation with application to computerized training of cryosurgery

Anjali Sehrawat · Kenji Shimada · Yoed Rabin

Received: 6 March 2012 / Accepted: 21 June 2012

Abstract
Purpose As a part of an ongoing project to develop computerized training tools for cryosurgery, the objective of the current study is twofold: to compile literature data on the likelihood of cancer tumor growth and its effect on the prostate shape and to present a deformation scheme for a 3D organ template in order to generate clinically relevant prostate models. The long-term objective of this study is to develop a database of prostate models for computerized training.
Methods Cryosurgery is typically performed on patients with localized prostate cancer found in stage T3 or earlier. The distribution of key geometric features likely to be found in the prostate at stage T3 is integrated into a 3D prostate template by employing the extended free-form deformation (EFFD) method. The applied scheme combines two steps: pre-selecting a set of geometric parameter values and manipulating the lattice control points until the prostate model meets the desired criteria.
Results Examples for model generation are displayed, based on two 3D prostate templates previously obtained from ultrasound imaging. These examples include selected cases with unilateral and bilateral stage T3 tumor growth, suitable for incorporation into a training database.
Conclusions EFFD is an efficient method for rapid generation of prostate models. The compiled criteria for model generation do not lead to a unique shape since the contours for template deformation are randomly selected. Nevertheless, these criteria do lead to shapes resembling cancer growth, as various growth histories can lead to a tumor characterized by the same key parameter values.

A. Sehrawat · K. Shimada · Y. Rabin (✉)
Department of Mechanical Engineering,
Carnegie Mellon University, Pittsburgh, PA 15213, USA
e-mail: rabin@cmu.edu

Keywords Cryosurgery · Computerized planning · Prostate · Cancer · Free-form deformation · Geometric modeling

Introduction

Cryosurgery is the destruction of undesired tissues by freezing. Minimally invasive cryosurgery is often performed by strategically placing an array of cryoprobes within a prespecified target region. In prostate cryosurgery, the target region can be the entire gland or a portion of it [1]. Key to cryosurgery success is the selection of a cryoprobe layout that maximizes destruction to the target region while minimizing cryoinjury to surrounding healthy tissues. An ideal cryoprobe layout would create a three-dimensional (3D) thermal field such that a selected isotherm matches perfectly to the outer surface of the target region. The selected isotherm could be the onset of freezing—closely related to the visualized frozen region by means of medical imaging, the lethal temperature—a temperature threshold below which maximum destruction is achieved or any other clinically relevant temperature [2].

Currently, cryoprobe placement is an art held by the cryosurgeon, based on the surgeon's own experience and accepted practices. Sub-optimal cryoprobe layout may leave areas in the target region untreated, lead to cryoinjury to healthy surrounding tissues, require an unnecessarily large number of cryoprobes, increase the duration of the surgical procedure, and increase the likelihood of post-cryosurgery complications, all of which affect the quality and cost of the medical treatment [3]. While early sporadic studies have been presented to optimize the cryoprobe layout [4–6], those studies have been based on traditional optimization techniques, where the associated computation cost prohibited reduction

Published online: 11 July 2012

to clinical practice. More recently, two alternative optimization techniques have been developed, known as force-field analogy [7] and bubble-packing [8–10], which accelerated the optimization process tremendously. Combined with an efficient numerical technique to simulate the bioheat transfer process of tissue freezing [11], computerized planning is closer than ever before to become a clinical reality.

While improved computation techniques, optimization methods, and computer hardware are likely to have an impact on computerized planning, an extension of this line of research can lead to computerized training and education associated with cryosurgery [12–14]. One can envision a virtual cryosurgery setup, where a trainee practices creating an optimal 3D thermal field to conform to a particular organ shape at various stages of cancer. Such a computerized tool may enable case studies of "what-if" scenarios and even reevaluation of past clinical procedures via a cryosurgery database. A computerized training tool is expected to shorten the clinician's learning curve, while providing a wider perspective on thermal effects and clinical practice. It has become the mission of the current research team to develop the building blocks necessary to make computerized training of cryosurgery a practical reality.

Beyond adequate computer resources, computerized training necessitates three key elements: a simulator of the procedure, a tutor to provide feedback on specific simulated cases, and a database to store case-specific information. The mainstay of the above key elements is the availability of high-quality organ models of candidates for cryosurgery [15]—the objective of the current study. The long-term goal in this line of study is to develop a database representative of the patient population undergoing cryosurgery. One approach to represent an abnormal growth of a prostate due to cancer tumors is by selecting a normal prostate model—a template—and deforming it to correspond with the progression of the disease. The challenges associated with generating a prostate model from a template originate from the intrinsic asymmetry of the organ and the variability in growth patterns exhibited in the population of prostate cancer patients. The current study is aimed at developing a computational technique for deforming a template model using extended free-form deformation (EFFD), while proposing a systematic approach for generating a database that is reflective of the prostate cryosurgery patient population.

Prostate cancer and tumor growth

Cancer staging is one of the primary prognostic measures used to determine an appropriate course of treatment. Prostate cancer is most often staged using the TNM classification system [16], which characterizes the severity of cancer based on the extent of the primary tumor (stage T), lymph nodes involvement (stage N), and metastasis (stage M). The T stage is further divided into four sub-stages: T1 and T2 correspond to cancer confined to the prostate gland; T3 corresponds to cancer tumors that have extended through the prostatic capsule and/or into the seminal vesicles, but have not spread into nearby tissue or organ; and T4 corresponds to cancer tumors that have spread into adjacent tissues. Cancer is considered to be localized if it is at stage T3 or lower and has not metastasized to local (N0) or distant lymph nodes (M0). The distribution of geometric features that are commonly found in the prostate at T3-stage cancer is presented below, where cryosurgery is typically performed on patients with stage T3 cancer or earlier [1,17,18].

The approach proposed in this study for determining critical tumor characteristics is based on surface changes caused by cancer penetrating through the prostatic capsule. Nevertheless, cancer confined within the capsule has the potential to alter prostate geometry, even in the early stages of cancer as T1 and T2. Tumors typically grow by invading adjacent tissue, which can replace glandular tissue, displace glandular tissue, or a combination of both [19], where glandular tissue displacement may also affect the prostate shape. Furthermore, prostate cancer can be multifocal, which presents a challenge in analyzing cancer-related prostate contour changes, as the overall shape of the organ may be affected by different deformation mechanisms at various locations.

Tumor size and location are the primary considerations for prognosis and subsequent selection of treatment. However, little attention has been paid to determining the relationship between tumor growth type and prostate shape changes. To the best of our knowledge, since prostate cancer treatments are mostly focused on excision, resection, or destruction of the tissue in situ, the effects of cancer growth type on the prostate shape have never been studied before. In a multifocal cancer, the primary tumor (i.e., the largest tumor) is most frequently used to define the cancer stage. About 80 % of non-primary tumors are of small volume (defined as less than 0.5 cc) and low grade (cells poorly resemble cancer cells according to the Gleason score), indicating that most of the non-primary tumors may not call for clinical intervention [20]. Relative to the average volume of the candidate prostate for cryosurgery (about 35 cc), those tumors would have negligible effects on the prostate shape.

It is noted that describing prostate geometry changes solely based on cancer growth is challenging as prostate cancer is often diagnosed in older men, with two-thirds of the cases above 65 years old [21]. This may further complicate the analysis of prostate shape changes since the prostate tends to enlarge with age naturally, but may also enlarge as it becomes more susceptible to other prostatic diseases such as benign hyperplasia [22]. In the current study, characterization of critical geometric features that affect a T3-stage prostate is based upon the assumption that only the primary

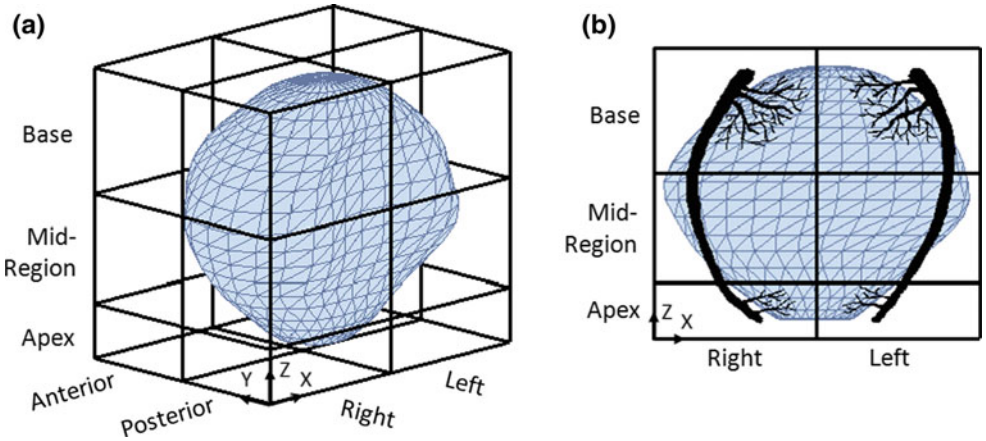

Fig. 1 Sectioned prostate template used in the current study to identify areas of cancer growth: **a** an *isometric view* and **b** *top view* showing the neurovascular bundle and superior and inferior pedicle. The notation on the x-axis refers to the patient's *left* and *right*, as it would be viewed by the clinician

tumor experiences extra-capsular extension (ECE). Here, the T3-stage cancer can be further classified as unilateral ECE, bilateral ECE, or spread into the seminal vesicles [23]. Only unilateral ECE and bilateral ECE are considered in the current study, since cryosurgery is routinely performed on prostates in which cancer is confined to the gland.

It has been observed that 68 % of cancer tumors are found in the peripheral zone of the prostate [24], which correlates with about 70 % of the prostate total volume [25]. Since the majority of tumors are found in the peripheral zone, clinical data used in the current study are restricted to cancer originating from this area, whereas follow-on studies are planned to address the remainder of the prostate. With reference to Fig. 1, peripheral-zone cancers typically spread laterally (x–y plane) along the nerve branches toward the posterolateral capsule, and vertically (z-direction) toward the superior pedicle along the base [26]. Therefore, shape changes in the current study are further restricted to the posterior mid-region and the base.

McNeal and Haillot [27] investigated 571 prostates removed during radical prostatectomy to evaluate cancer growth patterns relative to cancer volume. Each prostate was dyed, preserved (fixed in formaldehyde), and then cut into 3-mm-thick slices along the transverse plane. Each slice was examined by means of microscopy to trace tumor and relevant prostate boundaries. Tumors were sorted by zone of origin and by tumor volume. Measurements related to tumor location (sub-capsular invasion) within the transverse plane, percent of prostate base and apex replaced by cancer, extent of tumor capsular penetration, and tumor volume were calculated using computer planimetry. Each measurement was taken on the transverse plane.

The results presented by McNeal and Halliot [27] do not fully describe the geometric effects of cancer on the prostate surface, but provide the values for key parameter listed above, as cancer tumors may take arbitrary shapes. Sub-capsular invasion relative to tumor volume are summarized separately from tumor extension at the prostate base relative to tumor volume. However, the combined effects of tumor sub-capsular invasion and tumor extension at the base relative to the tumor volume have not been specified. Based on that study, it follows that one may predict the percentage of tumors of a specific volume that occur at a specific location, but may not know the likelihood of all possible tumor volumes occurring at the same location. Additionally, the location of tumor extension on the transverse plane has not been clearly assessed.

Figure 2 displays the statistical distribution of extra-capsular extension (ECE) based on tumor volume and tumor location, as compiled in the current work from the study of McNeal and Halliot [26], while integrating the topographical anatomy of periprostatic and capsular nerves, as quantified by Ganzer et al. [28]. The compiled data presented in Fig. 2 serve as the mainstay in developing a strategy to construct a database for candidate prostates for cryosurgery (up to T3-stage cancer). Selection of model parameters for demonstration purposes in the current study is presented below, whereas database construction is a task left to be performed in concert with the tutoring code development [12,14].

For demonstration purposes, two healthy prostate templates are used in the current study that represent the average and the maximum prostate volume of cryosurgery patients, 35 and 50 cc, respectively. McNeal and Haillot [27] found that ECE was more prevalent in tumors larger than 4 cc; therefore, this study assumes that a prostate at T3-stage cancer is likely to have tumors larger than 4 cc. For those tumors, ECE was observed primarily at the base of the prostate and was most frequently associated with cancer spread extensively along extra-prostatic nerves of the superior pedicle (see Fig. 1b). Consistent with the specific volume information presented in

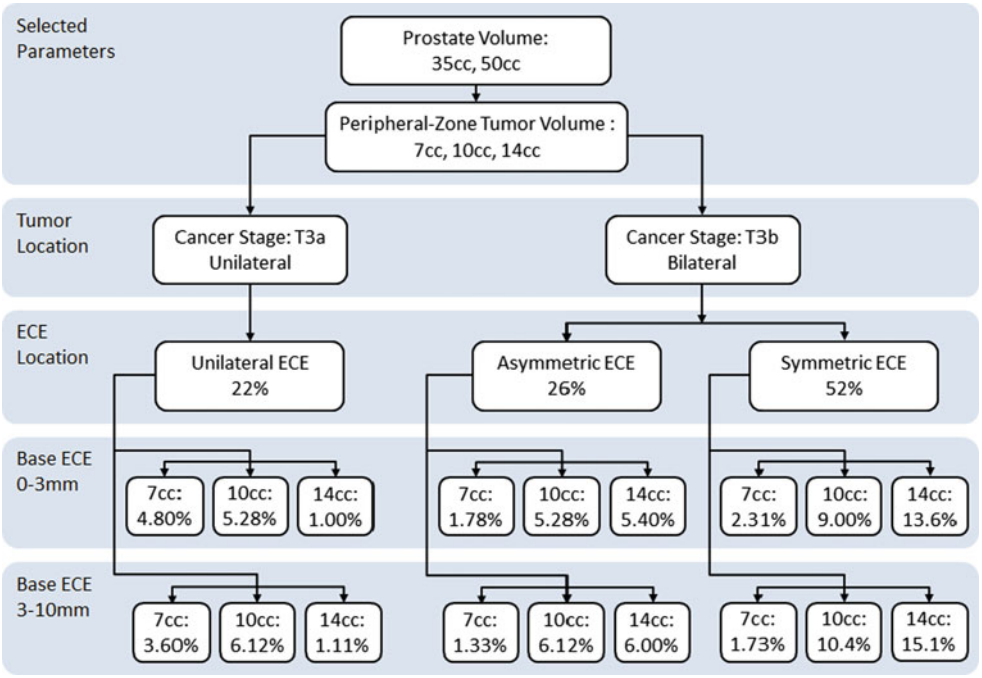

Fig. 2 Statistical distribution of extra-capsular extension (ECE) based on tumor volume and tumor location selected in the current study for database generation; data were compiled from [27,28]

[27], three representative tumor volumes are selected in the current study: 7, 10, and 14 cc. The relative distribution of each of those representative tumor volumes in the stage T3 cancer patient population is unknown, as there is no direct correlation between tumor volume and cancer staging. In the absence of more specific information, the model presented in this study does not assume higher likelihood of finding any particular tumor volume in stage T3 cancer. Furthermore, the primary concern in constructing a prostate model for cryosurgery planning is capturing surface changes that result from the extra-capsular tumor extension, and therefore the actual tumor volume is of lower importance since majority of the tumor lies within the prostate.

Location and extent of prostatic capsular extension are further attributed to each representative tumor volume, as displayed in Fig. 2. Tumor location is determined by its sub-capsular invasion, which can be either unilateral or bilateral. Unilateral tumors are characterized by tumor sub-capsular invasion extending to and slightly beyond the midline. For these tumors, ECE remains on the lobe of origin. Bilateral tumors are further divided into two groups: asymmetric ECE and symmetric ECE. Asymmetric ECE extends past the midline, but is primarily on the lobe of origin. Symmetric ECE is defined by tumor extension beyond the prostatic capsule on both lobes. For each tumor volume, 22, 26, and 52 % of occurrences were found to have unilateral ECE, bilateral-asymmetric ECE, and bilateral-symmetric ECE, respectively [27,28]. Both sub-capsular invasion and extra-prostatic nerve distribution were used to tabulate the ECE location percentages because cancer tends to spread along the extra-prostatic nerves.

For peripheral zone cancer, three base ECE configurations are possible: (1) left or right unilateral, (2) left or right bilateral-asymmetric, or (3) bilateral-symmetric. Tumors are equally likely to originate from the left or the right lobe [29]. Each ECE configuration at each location is associated with a transverse span along the prostate perimeter, based on extra-prostatic nerve distribution. Ganzer et al. [28] took transverse slices of prostate specimens, which were removed during non-nerve-sparing radical prostatectomy and dissected them into 12 evenly spaced sections in order to determine the extent of extra-prostatic nerve surface area within each section. The same sectioning scheme has been adopted in the current study to match each ECE configuration with a transverse span. Each span is composed of a set of sections that encompass the prostate perimeter with respect to the tumor location, where extra-prostatic nerves are likely to be found. It follows that for each ECE configuration, the corresponding transverse span defines the area along the prostate surface where ECE is likely to be found.

Figure 3 displays a transverse cross section (x–y plane) of the prostate template divided into 12 sections. The transverse spans coupled with left unilateral and bilateral-asymmetric ECE configuration are associated with section numbers 2–6 and 2–8, respectively; right unilateral and bilateral-asymmetric ECE configuration are associated with section numbers 7–11 and 5–11, respectively. Sections 2–11 are associated with the transverse span of bilateral-symmetric ECE

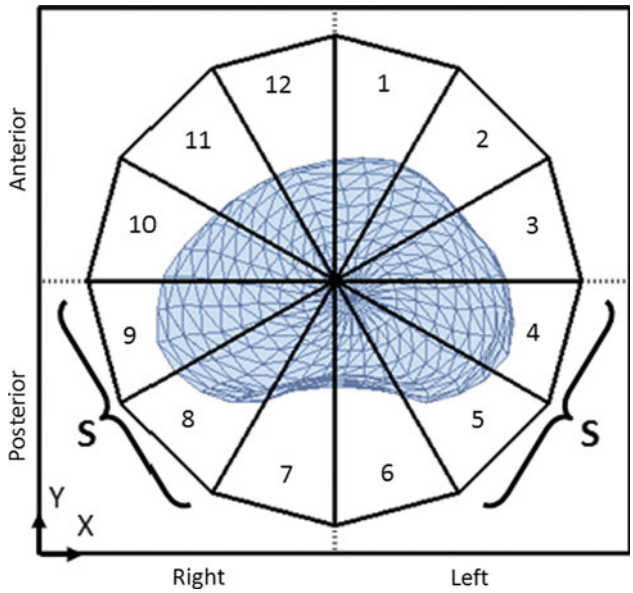

Fig. 3 Transverse sectioning of the prostate, where *S* represents regions along prostate base with highest extra-prostatic nerve density, found in the posterolateral ends of the prostate as displayed in Fig. 1

configurations. The section pair labeled with *S* represents the region with the highest concentration of nerves to surface area, which correlates with 84.1 % of the total extra-prostatic nerve surface area [28]. Based on the ECE location, tumors are likely to penetrate the capsule wall along the transverse span with maximum extension in region *S*.

For each ECE location, the likelihood that a tumor will extend beyond the prostate capsule are 48 and 52 % for extensions of 0–3 mm and 3–10 mm, respectively [27]. The percentage of 7, 10, and 14 cc tumors calculated to extend 0–3 and 3–10 mm beyond the prostate capsule for each ECE location is presented in Fig. 2. Based on the data summarized above, critical tumor features—ECE location and ECE length—were selected for the development of a prostate-model database for cryosurgery candidates.

Computational technique

This study applies extended free-form deformation (EFFD) on a 3D prostate template, using a modified computational technique [30]. The EFFD method is an extension of Sederburg's free-form deformation (FFD) method [31], where the deformation is applied to the space in which an object is embedded, rather than directly to the object.

Numerous studies have developed computational methods that apply FFD to a template object, to create patient-specific 3D anatomical models based on a set of 2D medical images such as those obtained from CT, MRI, SPECT, and X-ray [32–35]. In these studies, FFD is applied through an optimization process to minimize either the distance or the cross-sectional area difference between contours found on the 2D images and the deformed model contour. Little attention has been paid to integrating clinical data into modeling of the prostate in order to create the exact shape of the cancerous prostate. In the current study, we attempt to generate realistic geometric models that are likely to be encountered by clinicians in typical cases of prostate cryosurgery. The current study uses EFFD and can be viewed as an extension of our pervious exploratory study [13], which employed the basic FFD method. Furthermore, our previous study [13] did not incorporate ECE nerve distribution to determine the likelihood of lateral tumor ECE location, nor did it include criteria for successful deformation.

The FFD method is presented here in brief, for the completeness of presentation. With reference to Fig. 4a, a local coordinate system is imposed on a parallelepiped region which can be used to describe any point X in the unit volume by:

$$X = X_0 + sS + tT + uU \tag{1}$$

where X_0 is the origin of the local coordinate system; S, T, U are unit vectors of the local coordinate system; and s, t, and u are given by:

$$(s,t,u) = \left(\frac{T \times U \cdot (X - X_0)}{T \times U \cdot S}, \frac{S \times U \cdot (X - X_0)}{S \times U \cdot T}, \frac{S \times T \cdot (X - X_0)}{S \times T \cdot U} \right) \tag{2}$$

where s, t, and u are in the range of 0 and 1.

A set of control points, P_{ijk}, are imposed on the parallelepiped region, where l, m, and n are the number of subdivisions along each of the unit vectors S, T, and U, respectively:

$$P_{ijk} = X_0 + \frac{i}{l}S + \frac{j}{m}T + \frac{k}{n}U \tag{3}$$

The control points are moved, and the displaced object vertices are determined using the trivariate Bézier function:

$$X_{ffd}(s,t,u) = \sum_{i=0}^{n}\sum_{j=0}^{m}\sum_{k=0}^{l} P_{ijk} B_i^n(s) B_j^m(t) B_k^l(u) \tag{4}$$

where $B_i^n(s)$ is the Bernstein polynomial given by:

$$B_i^n(s) = \binom{n}{i} s^i (1-s)^{n-i} \tag{5}$$

Although FFD is a powerful modeling technique, its main disadvantage is that the types of deformation that can be created are restricted by the parallelepiped shape of the lattice. The FFD method discussed in this paper refers to the case where the entire object is embedded in a single control grid and the FFD deforms the object globally; here, one control point movement affects the entire surface of the object. By contrast, EFFD allows the user to create localized deformations of an arbitrary shape on the object surface [36].

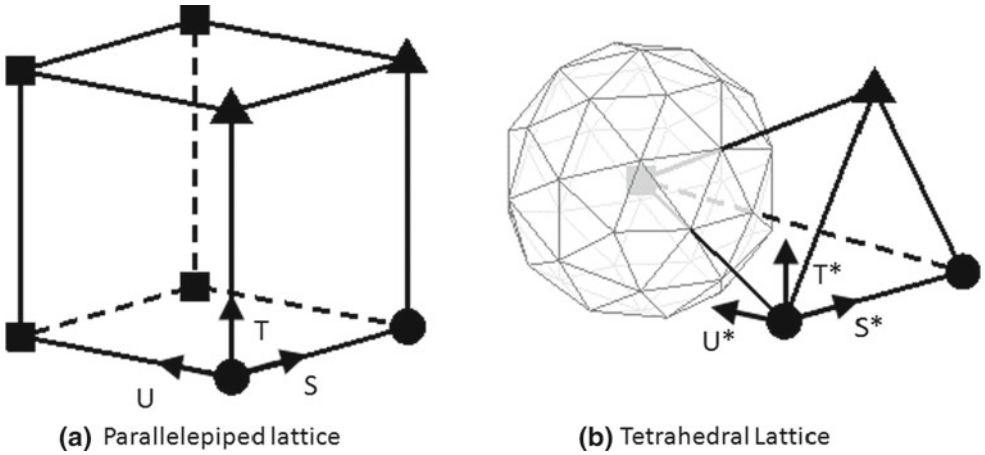

Fig. 4 Tetrahedral lattice is formed by merging two sets of points on the parallelepiped lattice. *Circle* is an unchanged control point. *Square* and *triangle* control points are merged

Non-parallelepiped lattices can be designed specifically for the deformation desired. The EFFD lattice is comprised of multiple FFD lattice structures. The object is embedded in the EFFD lattice, and deformation is passed only onto the object surface that lies within the individual FFD lattices associated with the displaced control point.

A spherical EFFD lattice composed of tetrahedral lattices was selected to deform the prostate-model template. A tetrahedral lattice is obtained by merging two sets of points of a parallelepiped lattice, as shown in Fig. 4. The primary challenge with implementing EFFD is calculating the parameterized coordinates (s, t, u) of the object in a non-parallelepiped space. Coquillart used a Newton approximation to calculate the coordinate [36]. MacCracken and Joy presented a FFD technique, which uses arbitrary lattices, namely, Catmull-Clark subdivision volumes [37]; but the lattice space definition is time-consuming and difficult, requiring a great deal of CPU time and memory. Xiao used a projection technique to calculate the parameterized coordinates in a cylindrical space [38]. The projection method has been modified in the current study to calculate the (s^*, t^*, u^*) coordinates in a tetrahedral lattice, an intermediate step in obtaining the (s, t, u) coordinates. The coordinate mapping process in the current study is described in the following steps:

1. Determine the center point of the triangle (tetrahedron face) that lies on the S^*T^* plane.
2. The line that connects the center point to the tetrahedron corner point in the center of the spherical EFFD lattice can be defined. The point can be projected onto this line. Calculate u from the ratio between the entire line length and the length obtained by the projected point.
3. Determine the triangle parallel to the S^*T^* plane, formed at the u coordinate of the point. Define the base and height of the triangle to be parallel to S^* and T^* axes, respectively.
4. Determine the width of the triangle at the point. Calculate s from the ratio between the width and the length obtained by projecting the point onto the width.
5. Project the point onto the triangle height. Calculate t from the ratio between the length of the height and the length obtained by the projected point.

Using the projection method, the object vertices (s^*, t^*, u^*) encompassed by the tetrahedron are mapped onto a rectangular solid, forming one-half of the parallelepiped lattice. The (s, t, u) coordinates are obtained by calculating the parameterized coordinates with respect to the entire parallelepiped lattice. Each control point moved is translated onto the parallelepiped lattice. The Bézier function can then be applied to determine the displaced object vertices in the parallelepiped space. The final deformed object vertices are obtained by mapping the displaced object vertices, calculated in the parallelepiped space, back onto the tetrahedron.

The spherical lattice is composed of 80 tetrahedrons and has 42 control points. Each tetrahedron is defined by 64 points; however, only 3 of the 4 corner control points are used to manipulate the object surface. The EFFD lattice is formed by merging the matching control points on neighboring tetrahedrons. Each control point moved on the EFFD lattice displaces adjacent control points within the corresponding lattice, as shown in Fig. 5. This maintains a smooth contour between surface deformations made from neighboring control points of the EFFD lattice.

The template 3D prostate shape is represented as a closed shell of a polygonal mesh, consisting of a set of vertices and a set of triangular faces. It is important that there be no gap or overlap between faces. Any gap or overlap will make it impossible to create a quality mesh for finite-element-based cryosurgery simulations. Also, the resolution of the template prostate should be sufficiently fine so that small features of its shape will still be visible after the template prostate geometry

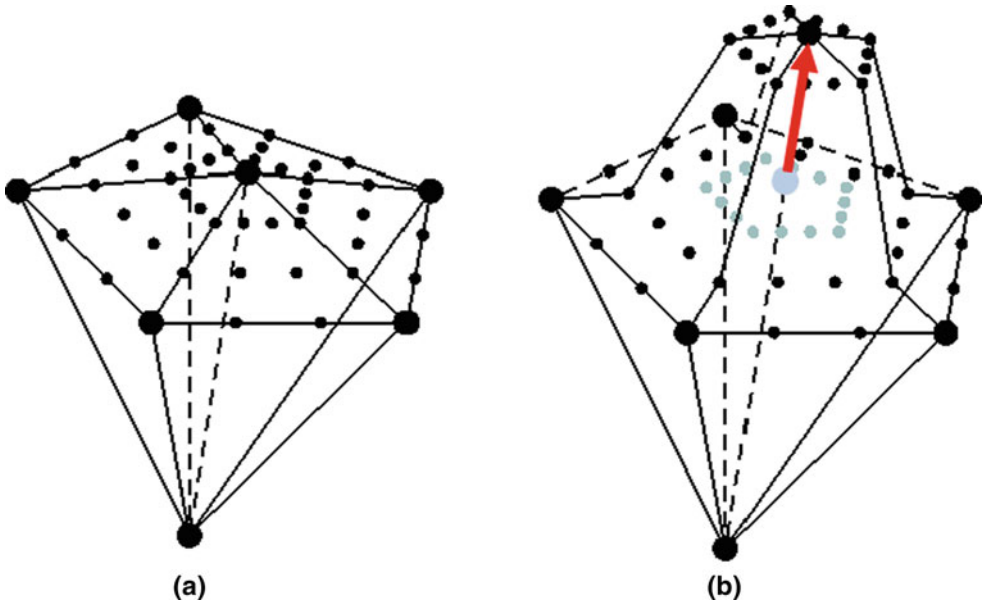

Fig. 5 Control point movement within each tetrahedral lattice. **a** A section of the spherical extended free-form deformation (EFFD) lattice with surface control points. *Large black dots* represent the control points available for manipulation, and *small black dots* represent the remaining control points within each tetrahedral lattice. **b** EFFD is carried out for each control point movement by displacing the neighboring control points (*gray dots*) an equal amount within each tetrahedral lattice

is deformed. The current template polygonal model consists of 581 vertices and 1,158 triangular polygons.

Deformations are carried out on a GUI, allowing the user to manually displace control points and instantaneously view the applied deformation on the template model. Figure 6 displays the basic framework of the code used to generate deformed prostate models along with the required user inputs. Deformation criteria used to generate prostate models are consistent with Fig. 2. Deformation is restricted to the posterior base and mid-region; therefore, only control points normal to these regions are moved. Starting from the distal end of the prostate template, the apex is defined to be 9 mm thick, mid-region is 18 mm thick, and the remaining volume is the base [27]. Both templates of 35 and 50 cc are sectioned in the same manner. For each deformed model, the volume, maximum ECE length and location are calculated. The ECE length is defined as the distance between the transverse template contour and deformed model contour. Given the iterative process of correlating linear movements of control point with volume deformation, successful deformation is considered when the deformed model meets the criteria listed in Fig. 6.

Results and discussion

The study of key parameters of tumor ECE presented by McNeal and Haillot [27] is unique and comprehensive, but provides only key geometrical features relevant to the current study: the location of the maximum extension, its magnitude, and the plane on which its maximum extension was measured (always in the transverse direction). This information is extremely significant for prostate cryosurgery, as the trans-rectal ultrasound (TRUS) transducer, commonly used to monitor prostate cryosurgery, provides raw imaging information on the same plane. Further qualitative information by McNeal and Haillot [27] suggests that the pattern of tumor growth correlates very well with the neural system of the gland. The topographical anatomy of periprostatic and capsular nerves have been thoroughly studied by Ganzer et al. [28], which enables us to link the tumor growth patterns with specific areas of the prostate, as summarized in Fig. 2.

When presenting a computational technique for geometrical representation of an organ, a comparison of results with a "ground truth" model would be highly commendable. Unfortunately, the actual shape of prostate tumors is not available in the literature. Not surprisingly, the actual shape of the extracapsular portion of the tumor is not reported in the literature; typical of cancer growth, the tumor contour may take virtually an infinite number of shapes. Hence, a "ground truth" model for the deformed ECE is nonexistent. Accordingly, one of the modeling objectives in the current study is to meet the experimental pathology parameters measured by McNeal and Haillot [27], while taking into account the likelihood of finding a tumor in specific areas of the prostate (Fig. 2). The credibility of the captured ECE in the deformed models can be evaluated by consultation with imaging experts, urologists, pathologists, or oncology experts, as routinely done by the current research team. More discussion on the topic is included at the end of the current section, along with an

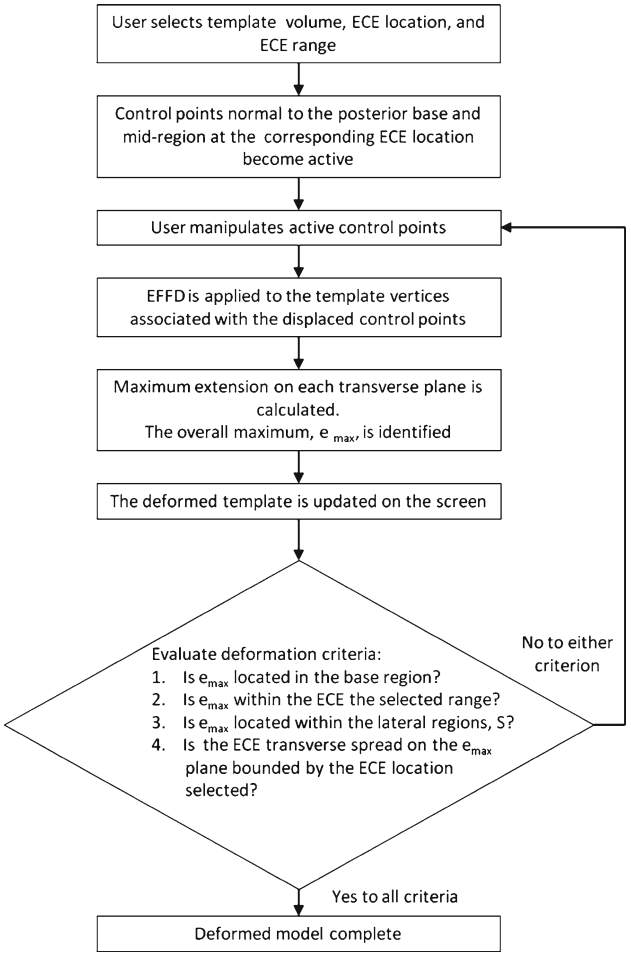

Fig. 6 A flow chart for the process of creating a prostate model from a prostate template

outlook on how the developed model may be integrated with cryosurgery training.

As described in the "Prostate cancer and tumor growth" section, two deformed models are presented in this section to demonstrate the application of the mathematical model, using a graphical user interface created with Matlab. The template for deformation has been developed in a previous study focusing on computerized planning of cryosurgery [8]; these templates have been created from 3D ultrasound data. Figure 7 displays a deformed model with right unilateral ECE. A 35cc template model was deformed to a volume of 36.8 cc. The selected ECE for this deformation was in the range of 3–10 mm (Fig. 2), where $e_{\max}$, defined as the maximum distance between deformed contour and template contour on any transverse plane, received a value of 5.3 mm. Figure 7b displays the transverse cross section of the prostate at $e_{\max}$. The highlighted region represents the maximum transverse span for the selected tumor location. The total ECE is confined to the transverse span specified for right unilateral ECE, with $e_{\max}$ located in the lateral region. Figure 7c shows that $e_{\max}$ is located at the base of the prostate model, at $z = 17$ mm.

Figure 8 displays a deformed model with symmetric ECE for the selected base ECE range of 0–3 mm. A 35cc template model was deformed to a volume of 36.9 cc. Figure 8c confirms that $e_{\max}$, 2.5 mm, is located at the base, at $z = 11$ mm. The total ECE is located within the maximum transverse span for the tumor location selected, and $e_{\max}$ is stationed in the lateral regions, as shown in Fig. 8b.

Figure 9 displays three examples of deformed models representing worst-case scenarios for prostate cryosurgery, having maximum ECE, $e_{\max}$, of 10 mm (Fig. 2). In general, the overall complexity of the prostate geometry increases with the extension size, making the cryosurgery procedure more challenging. The models in Fig. 9a, c exhibit left unilateral ECE and right bilateral-asymmetric ECE, respectively.

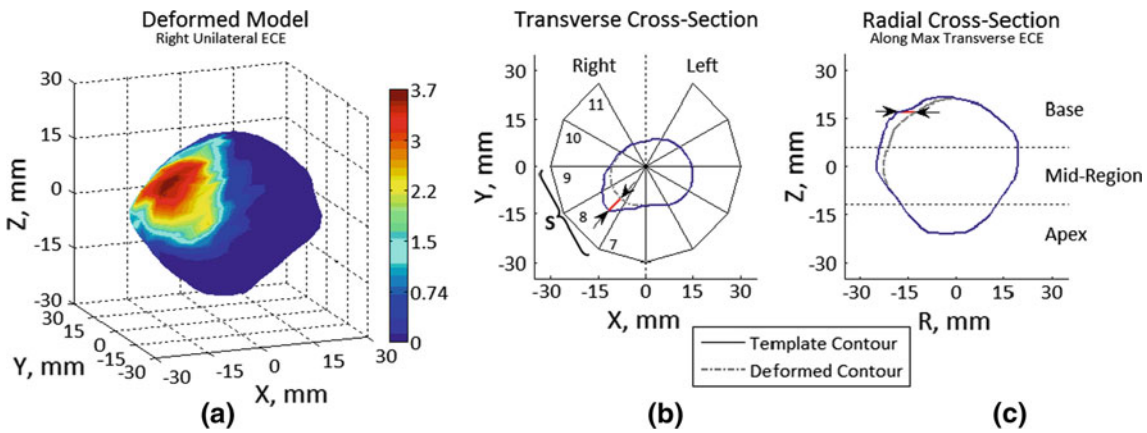

Fig. 7 An example of a prostate model created by the Tutor, following the flow chart illustrated in Fig. 6: **a** 3D view of right unilateral ECE, **b** transverse contour on a cross section at a depth of 17 mm, and **c** radial contour defined as the cross section perpendicular to the transverse plane along the maximum ECE

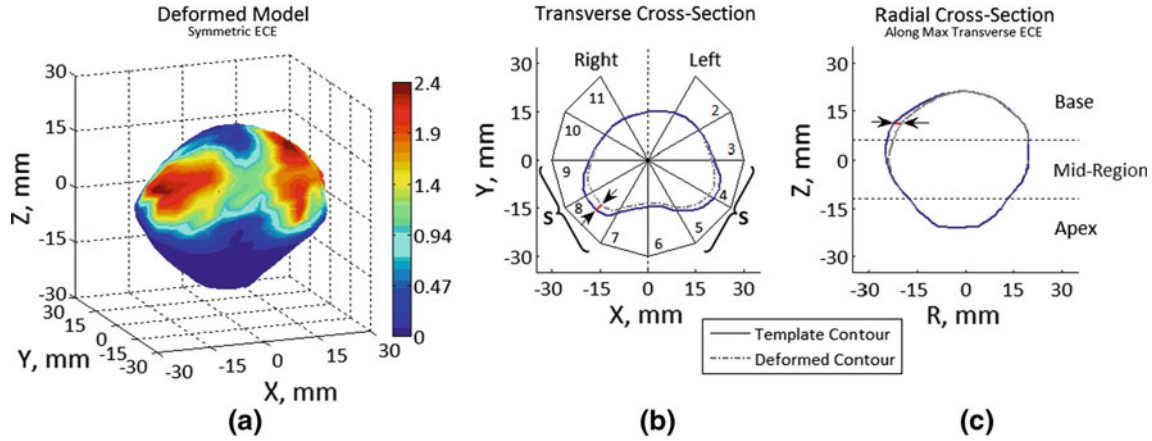

Fig. 8 An example of a prostate model created by the Tutor: **a** 3D view of symmetric ECE, **b** transverse contour on a cross section at a depth of 11 mm, and **c** radial contour defined as the cross section perpendicular to the transverse plane along the maximum ECE

Both were created using an initial template volume of 50 cc, eventually leading to deformed volumes of 51.9 and 52.2 cc, respectively. The model displayed in Fig. 9e was created from a 35cc template, eventually resulting in a volume of 38cc, after demonstrating a bilateral-symmetric ECE.

These models were generated by first selecting the desired deformation parameters—base ECE range and ECE location—and then manipulating the lattice control points until the deformed prostate-model ECE length and transverse span fell within the selected range. It is noted that the selected criteria for deformation do not lead to a unique deformed body. Interestingly, different cancer growth histories may also lead to a similar outcome of a specific size but different local features. Hence, a random deformation approach is selected to guide database construction, which is consistent with that of tumor growth. Randomized parameters are $e_{\max}$, transverse span and of the deformed region, and contour of the deformed region.

While the general technique used to deform the template model is well established, an original contribution in this research is in integration of prostate geometry with prostate cancer growth pattern and tailoring the deformation technique to generate the specific prostate models. The objective in the current study is to replicate the experimental results, with an emphasis on tumors at T3-stage cancer, by using the computational technique outlined above in the particular plane that the experimental data were measured. As discussed in the previous section, similar computational techniques [32–35] have been developed to generate 3D models of anatomical structures, using datasets composed of multiple 2D medical images containing cross sections of the target structure. In these studies, deformation is guided by an optimization process that aims at minimizing the distance or cross-sectional area difference between the 2D image contour and the model contour at the corresponding plane. In the current study, such detailed information is not available, and therefore, optimization is not integrated into the current modeling process. In the current study, the problem is underconstrained, and there is an infinite number of deformation patterns that could give the same distance or cross-sectional area difference. Hence, there is no guarantee that any other method from the literature will produce superior results for the purpose of quantitative comparison.

Lastly, an outlook on the integration of the proposed method with thermal surgery training is briefly discussed. A key difficulty in cryosurgery simulations and training is the lack of a credible target region to be destroyed by freezing [15]. This difficulty is not unique to cryosurgery simulations and training, but common in the training of other minimally invasive energy-based therapies, such as brachytherapy (local radiation therapy using radiation seeds), local hyperthermia by means of laser probes, thermal ablation by means of high-frequency ultrasound (HIFU), and the emerging application of hyperthermia using nanoparticles in an alternating magnetic field.

While the development of a training software is a major challenge, far extending the scope of the current study, three relevant key issues are inherent to the minimally invasive energy-based therapies listed above: (i) identifying the guiding principles to treat a typical target region (the prostate base case in the current study), (ii) exploring how the target region may evolve with the progression of the disease, and (iii) evaluating how changes in the target-region shape with the progression of the disease may affect the practice of the specific minimally invasive procedure.

While many criteria affect the success of minimally invasive cryosurgery, it is typically associated with matching some planning isotherm with the target-region shape, such as the onset of freezing, completion of freezing, or the so-called lethal temperature—a temperature threshold below which maximum destruction is achieved. In brachytherapy, a radiation dose region is typically matched with the target-region

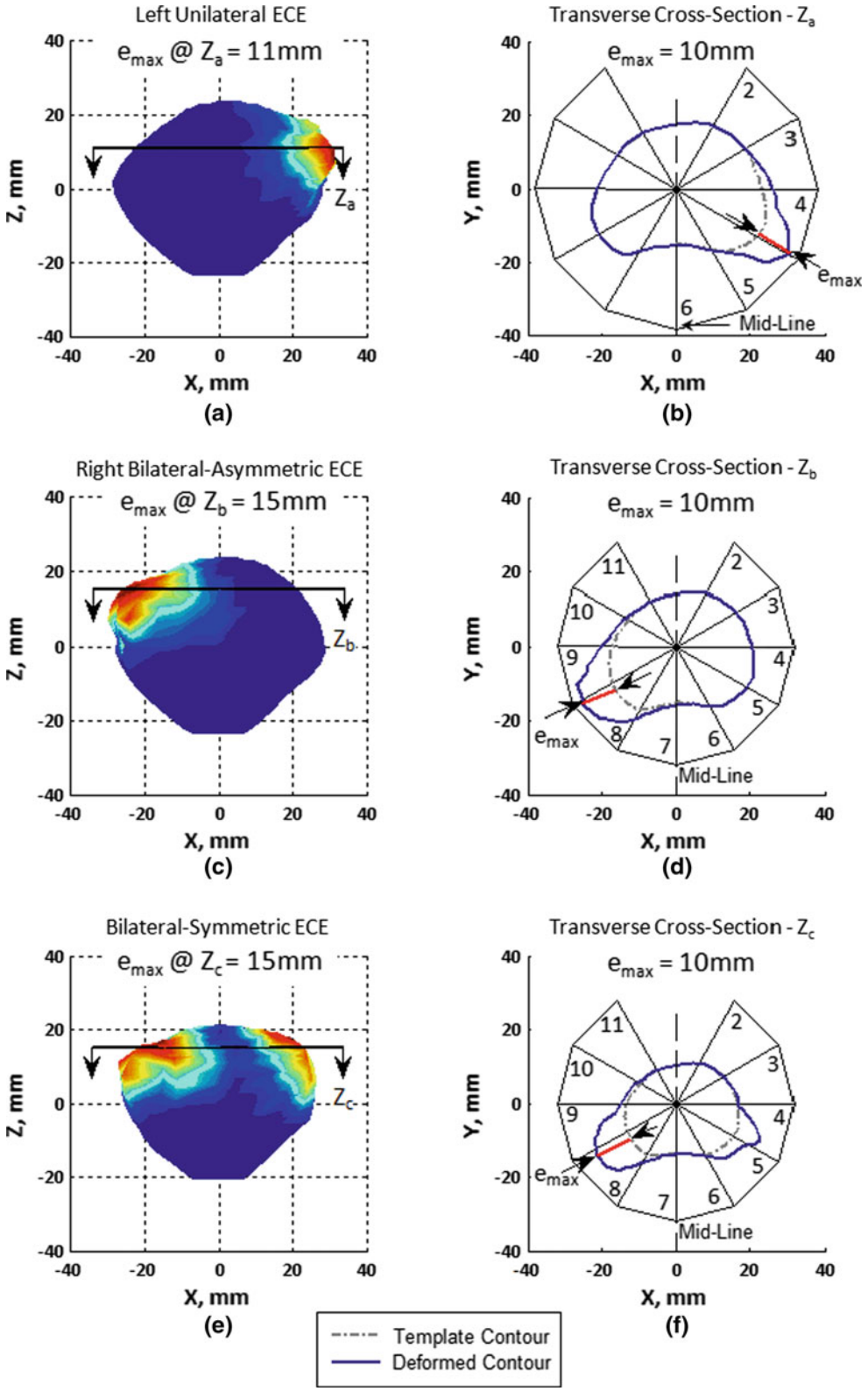

Fig. 9 Selected case study results. Case I represents a deformed 50 cc prostate template with left unilateral ECE: **a** *top view* and **b** corresponding transverse cross section at maximum ECE. Case II represents a deformed 50 cc prostate template with right bilateral-asymmetric ECE: **c** *top view* and **d** corresponding transverse cross section at maximum ECE. Case III represents a deformed 35 cc prostate template with symmetric bilateral-asymmetric ECE: **e** *top view* and **f** corresponding transverse cross section at maximum ECE

shape. Similarly, a thermal dose region is typically matched with the target-region shape in hyperthermic applications. Surgical planning of all of the above applications relies on computer simulations.

The computational method proposed in the current study can be integrated into computerized training in three primary ways: (i) to enable a "walk-through" demonstration of changes in the gland with the progression of the disease, (ii) to enable demonstration of how changes in the target-region shape affect changes in the energy sources layout (cryoprobes in the case of cryosurgery for example), and (iii) to create a database of prostate models having the same statistical distribution of candidates for the particular thermal surgery. For the latter application, automation can be employed in creating template deformations. For the latter two applications, computer-generated surgical planning [3,7–15] can be compared with interactive trainee operation, where the differences are automatically quantified, while the entire process is monitored by an experienced clinician. Either way, medical training is not perceived as an independent study, and the presence of an experienced surgeon should provide additional feedback on the virtual operation, including the credibility of the computer- generated shapes.

Conclusions

This study presents a review of critical geometric variations commonly found in patients with prostate cancer, with emphasis on T3-stage cancer, which represents the candidate population for prostate cryosurgery. The cancer growth pattern was characterized to provide basic guidelines for deforming a prostate template to develop clinically relevant 3D prostate models, in efforts to establish a training database representative of the patient population undergoing cryosurgery. The EFFD method was demonstrated as an effective computational technique for generating these prostate models.

The current study focuses on key geometrical features relevant to the extension of cancer tumors through the prostate capsule: the location of the maximum extension, its magnitude, the spread of the tumor on the prostate surface, and the plane on which its maximum extension was measured. This information is extremely significant for prostate cryosurgery, as the TRUS transducer commonly used in prostate cryosurgery provides raw imaging information on the same plane. Consistent with the random nature of the progression of the disease, the actual shape of the extended portion of the cancer tumor is not reported. Hence, a "ground truth" model for the deformed ECE is nonexistent. Integrating this random behavior, while maintaining the key geometrical features listed above, is perceived as a plausible approach to describe cancer tumor growth. Nevertheless, the creditability of the generated ECE has been discussed with clinicians in the course of the current study and will be evaluated in future applications by a mentor/experienced clinician.

It is essential to recognize that the deformation process involved in generating realistic prostate models has multiple facets. The deformation approach presented in this study addresses the localized changes that occur as a result of cancer on the prostate surface. However, in order to fully elucidate the variable shape of the prostate, which naturally differs from patient to patient, deformation must also be applied more broadly to include the entire prostate surface. Follow-up studies are planned to expand the current deformation approach in the global irregularities of prostate shape and to broaden the template base used in the current study for demonstration purposes. Demonstrations in the current study are based on two prostate templates, where more templates will be included in the actual process of database construction.

Acknowledgments This study was supported by Award Number R01CA134261 from the National Cancer Institute. The content is solely the responsibility of the authors and does not necessarily represent the official views of the National Cancer Institute or the National Institutes of Health.

Conflict of interest None.

References

1. Babaian RJ, Donnelly B, Bahn D, Baust JG, Dineen M, Ellis D, Katz A, Pisters L, Rukstalis D, Shinohara K, Thrasher JB (2008) Best practice statement on cryosurgery for the treatment of localized prostate cancer. J Urol 180(5):1993–2004
2. Gage AA, Baust J (1998) Mechanisms of tissue injury in cryosurgery. Cryobiology 37(3):171–186
3. Rossi MR, Tanaka D, Shimada K, Rabin Y (2008) Computerized planning of cryosurgery using bubble packing: an experimental validation on a phantom material. Int J Heat Mass Transf 51:5671–5678
4. Baissalov R, Sandison GA, Donnelly BJ, Saliken JC, McKinnon JG, Muldrew K, Rewcastle JC (2000) A semi-empirical treatment planning model for optimization of multiprobe cryosurgery. Phys Med Biol 45(5):1085–1098
5. Baissalov R, Sandison GA, Reynolds D, Muldrew K (2001) Simultaneous optimization of cryoprobe placement and thermal protocol for cryosurgery. Phys Med Biol 46(7):1799–1814
6. Keanini RG, Rubinsky B (1992) Optimization of multiprobe cryosurgery. J Heat Transf T ASME 114:796–802
7. Lung DC, Stahovich TF, Rabin Y (2004) Computerized planning for multiprobe cryosurgery using a force-field analogy. Comput Methods Biomech Biomed Eng 7(2):101–110
8. Tanaka D, Shimada K, Rabin Y (2006) Two-phase computerized planning of cryosurgery using bubble-packing and force-field analogy. ASME J Biomech Eng 128(1):49–58
9. Tanaka D, Shimada K, Rossi MR, Rabin Y (2008) Computerized planning of prostate cryosurgery with pullback procedure. Comput Aided Surg 13(1):1–13
10. Tanaka D, Rossi MR, Shimada K, Rabin Y (2007) Towards intraoperative computerized planning of prostate cryosurgery. Int J Med Robot Comput Assist Surg 3:10–19

11. Rossi MR, Tanaka D, Shimada K, Rabin Y (2007) An efficient numerical technique for bioheat simulations and its application to computerized cryosurgery planning. Comput Methods Programs Biomed 85(1):41–50
12. Keelan R, Shimada K, Rabin Y (2011) Developing a framework for computerized training of cryosurgery based on finite elements analysis. In: ASME summer bioengineering conference, Farmington, PA, USA
13. Sehrawat A, Shimada K, Rabin Y (2011) Geometric deformation of three-dimensional prostate model with applications to computerized training of cryosurgery. In: ASME summer bioengineering conference, Farmington, PA
14. Furuhata T, Song I-H, Rabin Y, Shimada K (2011) Interactive prostate shape reconstruction from 3D TRUS images. Int J Comput Assist Radiol Surg. (Submitted)
15. Rabin Y (2008) Key issues in bioheat transfer simulations for the application of cryosurgery planning. Cryobiology 56(3):248–250
16. Chang SS, McKiernan JM et al (2010) Genitourinary. In: Edge SB, Byrd DR, Compton CC et al (eds) AJCC cancer staging manual. 7th edn. Springer, New York, pp 457–468
17. Zisman A, Pantuck AJ, Cohen JK, Belldegrun AS (2001) Prostate cryoablation using direct transperineal placement of ultrathin probes through a 17-gauge brachytherapy template-technique and preliminary results. Urology 58(6):988–993
18. Han KR, Cohen JK, Miller RJ et al (2003) Treatment of organ confined prostate cancer with 3rd generation cryosurgery: preliminary multi-center experience. J Urol 170(4):1126–1130
19. Kohn EC (2010) Invasion and metastases. In: Hong WK, Bast RC, Hait WN et al (eds) Holland-Frei cancer medicine. 8th edn. PMPH, China pp 141–148
20. Meiers I, Waters DJ, Bostwick DG (2007) Preoperative prediction of multifocal prostate cancer and application of focal therapy: review 2007. Urology 70:3–8
21. American Cancer Society. http://www.cancer.org/Cancer/ProstateCancer/DetailedGuide/prostate-cancer-key-statistics. Accessed 19 Dec 2011
22. Bosch JL, Tilling J, Bohnen AM, Bangma CH, Donovan JL (2007) Establishing normal reference ranges for prostate volume change with age in the population-based Krimpen-study: prediction of future prostate volume in individual men. Prostate 67:1816–1824
23. National Cancer Institute. http://www.cancer.gov/cancertopics/pdq/treatment/prostate/Patient/page2. Accessed Jan 2012
24. McNeal JE, Redwine EA, Freiha FS, Stamey TA (1988) Zonal distribution of prostatic adenocarcinoma. Correlation with histologic pattern and direction of spread. Am J Surg Pathol 12(12):897–906
25. Bostwick DG, Qian J, Hossain D (2008) Non-neoplastic diseases of the prostate. In: Bostwick DG, Cheng L (eds) Urologic surgical pathology. Elsevier Inc, China, pp 381–442
26. Villers A, McNeal JE, Redwine EA Freiha FS, Stamey TA (1989) The role of perineural space invasion in the local spread of prostatic adenocarcinoma. J Urol 142(3):763–768
27. McNeal JE, Haillot O (2001) Patterns of spread of adenocarcinoma in the prostate as related to cancer volume. Prostate 49(1):48–57
28. Ganzer R, Blana A, Gaumann A, Stolzenburg J-U, Rabenalt R, Bach T, Wieland WF, Denzinger S (2008) Topographical anatomy of periprostatic and capsular nerves: quantification and computerised planimetry. Eur Urol 54(2):353–360
29. Opell MB, Zeng J, Bauer JJ, Connelly RR, Zhang W, Sesterhenn IA, Mun SK, Moul JW, Lynch JH (2002) Investigating the distribution of prostate cancer using three-dimensional computer simulation. Prostate Cancer Prostatic Dis 5(3):204–208
30. Shim M-B, Gunay M, Shimada K (2009) Three-dimensional shape reconstruction of an abdominal aortic aneurysm form computer tomography images using extended free-form deformation. Comput Aided Des 41(8):555–565
31. Sederberg TW, Parry SR (1986) Free-form deformation of solid geometric models. ACM SIGGRAPH Comput Graph 20(4):151–160
32. Gunay M, Shim M-B, Shimada K (2008) Cost- and time-effective three-dimensional bone-shape reconstruction from X-ray images. Int J Med Robot Comput Assist Surg 3(4):323–335
33. Bardinet E, Cohen LD, Ayache N (1995) A parametric deformable model to fit unstructured 3d data. INRIA, technical report 2617
34. Montagnat J, Delingette H (1997) Globally constrained deformable models for 3D object reconstruction. Signal Process 71(2):173–186
35. Battle XL, Le Rest C, Turzo A, Bizais Y (2009) Three-dimensional attenuation map reconstruction using geometrical models and free-form deformations. IEEE Trans Med Imaging 19(5):404–411
36. Coquillart S (1990) Extended free-form deformation: a sculpturing tool for 3D geometric modeling. ACM SIGGRAPH Comput Graph 24(4):187–196
37. MacCracken R, Joy KI (1996) Free-form deformations with lattices of arbitrary topology. In: Proceedings of the 23rd annual conference on computer graphics and interactive techniques, pp 181–188
38. Xiao Y. (2011) Extended free-form deformation. University of California, Santa Cruz. http://www.cse.ucsc.edu/classes/cmps260/Winter03/proj/yx51866/projectReport.html. Accessed 19 Dec 2011